Nuclear Instruments and Methods in Physics Research A 1086 (2026) 171319

Contents lists available at ScienceDirect

Nuclear Inst. and Methods in Physics Research, A

journal homepage: www.elsevier.com/locate/nima

Fabrication and performance testing of a metal photocathode pulsed X-ray tube prototype based on microchannel plate

Xiushan Wang [a], Yunpeng Liu [a,b,*], Kang Wang [a], Ziyao Zeng [a], Xiaobin Tang [a,b,**]

[a] Department of Nuclear Science and Technology, Nanjing University of Aeronautics and Astronautics, Nanjing, 210016, China
[b] Key Laboratory of Advanced Nuclear Technology and Radiation Protection, Ministry of Industry and Information Technology, Nanjing, 210016, China

ARTICLE INFO

Keywords:
Metal photocathode pulsed X-ray tube
Microchannel plate
Photocathode optimization
Current gain
Pulsed X-ray modulation

ABSTRACT

In this study, we report the fabrication and characterization of a prototype metal photocathode pulsed X-ray tube (MPPXT) integrated with a microchannel plate (MCP) structure. Key structural parameters of the X-ray tube were optimized using CST Particle Studio and the Non-dominated Sorting Genetic Algorithm II (NSGA-II), which we applied to guide the fabrication of the prototype. Au photocathodes with various deposition times were characterized, with a deposition time of 150 s yielding a maximum photocurrent of 20.45 nA. When the optimal Au photocathode was integrated into the prototype, the electron multiplication characteristics of both single- and dual-MCP configurations in an X-ray tube were systematically characterized for the first time. The single-MCP configuration at 1000 V achieved a tube current of 35 μA, with a current gain of ~1.76×10^3. The dual-MCP configuration at 1800 V further improved the multiplication efficiency, producing a tube current of 223 μA with a gain of ~1.17×10^4. Imaging experiments showed a minimum focal spot size of 0.27 × 0.47 mm, which was consistent with simulations. Moreover, the MPPXT achieved stable pulse modulation at 2 MHz. Thus, the proposed MPPXT exhibited enhanced output intensity and offered the advantage of convenient high-speed modulation. These results demonstrate that the proposed method is promising for applications in high-speed imaging, X-ray communication, and scintillator time-response measurements.

1. Introduction

With advances in science and technology, continuous X-ray sources no longer meet the demands of certain high-resolution applications such as X-ray communication, high-speed imaging, and scintillator time-response measurements. Pulsed X-ray tubes (PXTs) have thus attracted considerable attention for their high spatiotemporal resolution and controllable emission. PXTs generate pulsed radiation by modulating cathode electron emission or X-ray switching. Based on their modulation mechanisms and structural characteristics, they are typically categorized as grid-controlled [1,2], field-emission [3–5], or photocathode-based [6,7]. Among these types, photocathode pulsed X-ray tubes (PPXTs) operate on the principle of photoemission and use photocathodes as electron sources. They offer superior performance, including convenient modulation and pulse widths of several hundred picoseconds. Combined with mature optical modulation technologies, they enable stable pulsed X-ray output with a high repetition rate, with broad prospects for ultrafast imaging and scintillator time-response characterization. In 1992, Hamamatsu Photonics introduced the N5084 PPXT, which achieved a pulse width of ~100 ps and a tube current of 50 μA and thus demonstrated the feasibility of this approach [8].

PPXTs can be classified into semiconductor and metal types based on the photocathode material. Semiconductor photocathodes (e.g., alkali antimonides) exhibit high quantum efficiency (QE > 0.1) [9,10], which enables mA-level tube currents. For instance, Timofeev et al. developed an alkali photocathode X-ray tube that achieved a current of 1 mA under 455-nm illumination, with a modulation rate of up to 0.8 MHz [11]. Zhang et al. proposed a pulsed X-ray tube based on an S20 (multi-alkali) photocathode that achieved a repetition rate of 12.5 MHz and a pulse width of 4 ns, which sufficed to enable precise measurements of scintillator decay [12]. However, semiconductor photocathodes are air-sensitive and require ultrahigh vacuum conditions (~10^{-8} Pa) to maintain stability and lifetime [13]. In contrast, metal photocathodes (e.g., Au, Cu) exhibit lower QE (10^{-5}–10^{-4}) [14,15] but provide faster response, excellent chemical stability, and longer lifetimes, which makes

* Corresponding author. Department of Nuclear Science and Technology, Nanjing University of Aeronautics and Astronautics, Nanjing, 210016, China.
** Corresponding author. Department of Nuclear Science and Technology, Nanjing University of Aeronautics and Astronautics, Nanjing, 210016, China.
E-mail addresses: liuyp@nuaa.edu.cn (Y. Liu), tangxiaobin@nuaa.edu.cn (X. Tang).

https://doi.org/10.1016/j.nima.2026.171319
Received 7 October 2025; Received in revised form 20 January 2026; Accepted 25 January 2026
Available online 26 January 2026

them more suitable for operation in ambient environments. Nevertheless, their low QE limits the output current to the nanoampere or even picoampere level, which restricts their application in PPXTs.

One approach to enhance the output current of metal photocathode pulsed X-ray tubes (MPPXTs) is to optimize the thickness of the metal photocathode to improve its QE [16,17]. Although previous studies have confirmed that the QE of metal photocathodes depends strongly on their thickness, a direct relationship between photocathode thickness and output tube current has not yet been systematically reported for MPPXTs. In contrast, the output current can also be increased by integrating an electron multiplication structure to compensate for the insufficient photocurrent. For example, NASA developed an Mg photocathode X-ray tube incorporating electron multiplication, which achieved sub-nanosecond pulses with output currents of only several tens of μA [18]. In 2021, Kamezawa et al. proposed a novel MPPXT employing a Mg-coated channel electron multiplier (CEM) and successfully demonstrated dynamic X-ray elastography of a breast phantom at a tube voltage of 30 kV, a tube current of 20 μA, and a modulation frequency of 115 Hz. Their results thus verified the feasibility of the technique [19]. Although CEMs can provide gains up to 10^9, their typical temporal response is on the order of several ns, which may limit the temporal resolution of the X-ray tube. In contrast, a microchannel plate (MCP) achieves electron gain via secondary electron emission within an array of microscopic channels. With an applied bias, electrons undergo repeated wall collisions, generating a secondary electron cascade and hence avalanche multiplication. The short transit distance in the channels can yield a small transit time spread (sub-nanosecond or picosecond-level), benefiting high-speed modulation. In 2018, the authors [20] proposed a laser-modulated pulsed X-ray source based on an MCP, and in 2024 [7] we constructed an MCP-MPPXT prototype in a dynamic vacuum system. This prototype achieved a tube current of 195 μA, 10 MHz modulation, and a pulse width of 50 μs for dynamic imaging. Nevertheless, the multiplication characteristics of different MCP configurations and the optimal thickness of metal photocathodes remain insufficiently characterized and require further systematic investigation.

In this work, we designed and implemented an MPPXT with an integrated MCP. Key structural parameters were optimized using CST Particle Studio (CST) combined with the Non-dominated Sorting Genetic Algorithm II (NSGA-II). Subsequently, the photocurrent characteristics of Au photocathodes with varying thicknesses were systematically investigated, and the MCP was adopted to enhance the electron flux and X-ray emission intensity. Finally, a prototype MPPXT was fabricated and tested in a dynamic vacuum system, and the multiplication performance of both single- and dual-MCP configurations was comprehensively characterized. The results demonstrate that the developed MPPXT provides a technical foundation for high-current X-ray sources with high modulation frequency, and the device shows great potential for applications in high-speed imaging and scintillator time-response measurements.

2. Simulation and optimization of MPPXT

2.1. Structure design of MPPXT

The proposed MPPXT consists of five primary components, including a UV light source, a metal photocathode, an MCP, a focusing electrode, and an anode assembly, as illustrated in Fig. 1. The UV light source is used to excite the metal photocathode to emit photoelectrons. The photocathode material is deposited as a thin film on the inner surface of an optical window to form a transmissive structure. The MCP is placed ~300 μm behind the photocathode to amplify the limited photoelectrons. The cylindrical focusing electrode generates an electrostatic field that confines electron trajectories and improves beam collimation. The anode assembly comprises a reflective anode target and an anode shield. This configuration ultimately produces X-rays with high brightness and low divergence from the reflective target surface.

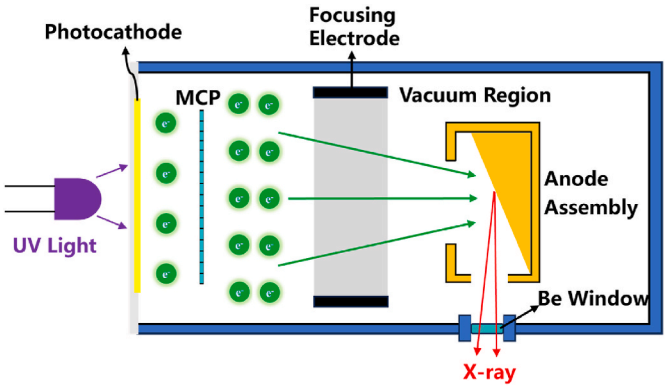

Fig. 1. Schematic diagram of the MPPXT.

2.2. Optimization of structural parameters

Electron bombardment—in which electrons accelerated by an electric field strike the anode—is a critical process in the operation of MPPXTs. The structural parameters of the focusing electrode and anode assembly strongly influence electron trajectories and their distribution on the anode surface and thus determine the quality of the output beam of X-rays. Optimizing these parameters allows control of the electron focal spot and enhances current density, which results in a small spot and high-brightness X-ray emission. Because an MCP contains millions of microchannels, full-scale modeling of the electron multiplication process is computationally prohibitive. Therefore, we focused only on simulating the electron transport process from the exit of the MCP to the anode target. CST was used to model the three-dimensional electromagnetic fields and to perform particle-transport simulations. Given the large number of structural parameters and the complexity of the objective functions, NSGA-II was adopted to address the multi-parameter, multi-objective optimization problem [21]. In this work, MATLAB acts as the workflow controller and couples CST and NSGA-II via CST's COM automation interface. NSGA-II proposes candidate decision variables, which MATLAB assigns to the CST parametric model to update the geometry and run simulations; MATLAB then extracts the objective values and passes them back to NSGA-II for the next generation. This iterative procedure continues until convergence, yielding a set of Pareto-optimal solutions [22]. The computational cost is dominated by CST evaluations and scales approximately with the product of the population size and the number of generations. With a 50 × 50 setting, 2500 CST runs are required, resulting in a total runtime of approximately 3 days, depending on the per-run simulation time and available computing resources.

In the simulation model, as shown in Fig. 2(a) and (c), the plane at z = 1 mm was defined as the MCP output surface, from which an electron source emitted 16,358 electrons. In Fig. 2(c), the electron transport trajectories toward the anode target are shown, where the color represents the electron kinetic energy (eV) on a linear scale and thus illustrates its evolution along the trajectories. To simplify the optimization and achieve an electrically safe clearance, the distance between the focusing electrode and the anode shield was fixed at 20 mm. The optimization parameters included the starting (*f_begin*) and ending positions (*f_end*) of the focusing ring, the inner radius (*f_in*), the focusing electrode voltage (*f_V*, not shown in the figure), the aperture radius of the anode shield (*s_aperture*), and the distance between the shield and the anode target (*shield_anode*). These served as decision variables in the NSGA-II optimization framework. Compared with our previous work [7], in which NSGA-II was used to optimize only the focusing electrode geometry and axial position while the anode structure was kept fixed, the present study further extended the optimization scope to jointly optimize the focusing electrode and the anode assembly (anode shield and anode target). Accordingly, the decision variables were expanded to

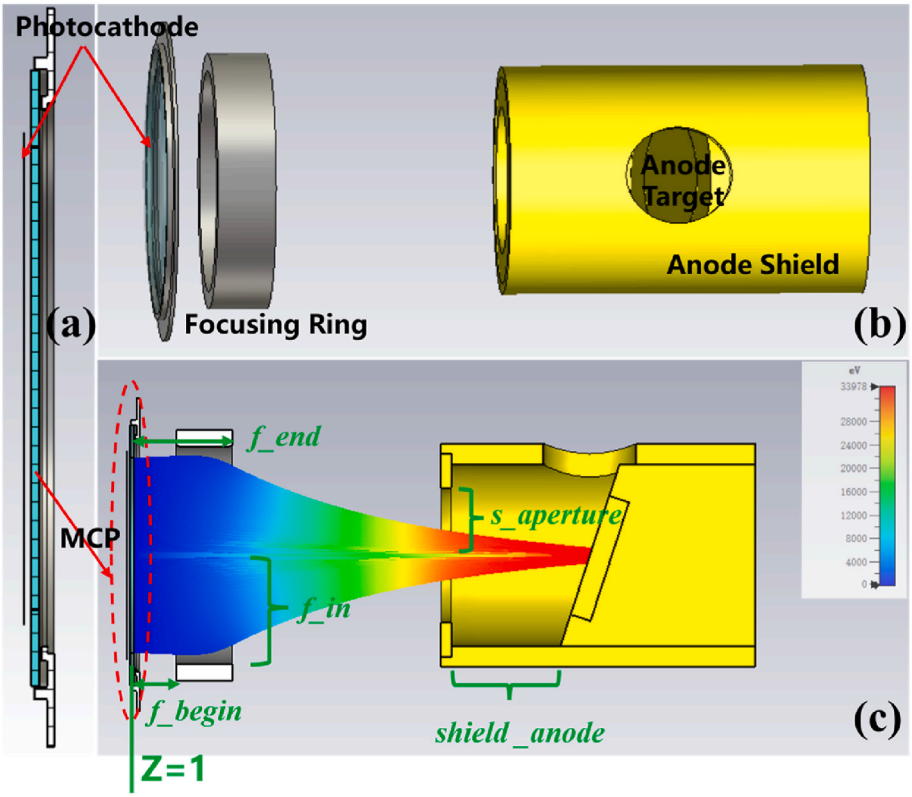

Fig. 2. Schematic diagrams: (a) Photocathode structure. (b) Simplified model of the MPPXT. (c) Electron transport trajectories and optimized structural parameters.

include the focusing electrode voltage and the anode assembly parameters (*s_aperture* and *shield_anode*), in addition to the focusing electrode geometry.

To enable a direct comparison with our previous work [7], the objective functions were kept the same, namely the anode electron collection efficiency (C_e), the electron focal spot radius (R_{EFSR}), and the electron transit time (*TT*). These parameters respectively represent electron transmission efficiency, spatial resolution, and temporal synchronization of the MPPXT. C_e is defined as the ratio of electrons collected on the anode monitoring surface to those emitted from the MCP, with an ideal value of $C_e = 1$. R_{EFSR} represents the scale of the electron focal spot on the anode monitoring surface and can be converted into the effective focal spot size of the X-rays (R_{XFSS}) by incorporating the anode target angle. *TT* refers to the time required for electrons to travel from the MCP surface to the anode monitoring plane and generate a peak output signal. With C_e constrained to 1, the optimization balanced R_{EFSR} and *TT* to determine the optimal structural parameter set. Table 1 compares the optimized structural parameters and corresponding simulation results between the present study and our previous work [7]. The optimized MPPXT in this work achieved a smaller focal spot and a shorter electron transit time, suggesting improved spatial and temporal performance. Fig. 3 compares the electron focal spot distribution on the anode monitoring surface before and after optimization. The pre-optimization case in Fig. 3(a) corresponded to an empirically selected baseline geometry based on our previous prototype design and was used to construct the initial model for the NSGA-II optimization. Compared with the baseline case, the post-optimization configuration (Fig. 3(b)) achieved an ideal C_e and exhibited significantly improved electron beam focusing with a markedly reduced focal spot size. Furthermore, the *TT* decreased from ~1 ns to ~0.69 ns after optimization, indicating a clear enhancement in temporal performance.

Table 1
Comparison of optimized parameters and simulation results of the MPPXT in the present work and in Ref. [7].

Parameter	This work	Ref. [7]
f_begin	4.54 mm	2.54 mm
f_end	9.48 mm	9.60 mm
f_in	10.41 mm	9.78 mm
s_aperture	6.92 mm	–
shield_anode	10.52 mm	–
f_V	2300 V	–
R_{XFSS}	0.08 × 0.13 mm	0.26 × 0.80 mm
TT	0.69 ns	0.87 ns

3. Fabrication and characterization of Au photocathodes

3.1. Preparation of Au photocathodes

Au was selected as the photocathode material because it provides stable photoelectron emission under the ultraviolet illumination conditions used in this study and is chemically stable in both ambient air and vacuum. This stability improves the repeatability of photocurrent measurements under vacuum conditions [7]. In addition, Au films can be reproducibly deposited by sputtering with well-controlled thickness, enabling a systematic study of thickness-dependent photoemission.

To fabricate the Au photocathodes, a Cr/Cu/Ag circular conductive film was deposited on a pre-cleaned single-crystal magnesium fluoride (MgF_2) substrate (32 mm in diameter, 3 mm thick, with an effective area diameter of 20 mm) using DC magnetron sputtering. This conductive layer served as the bias electrode for the subsequent metal photocathode. Prior to the deposition of the photocathode material, the substrate was cleaned to remove residual moisture and hydrocarbons. After cooling, an Au thin film was deposited on the substrate via ion sputtering. Argon (Ar) gas supplied a working pressure of 5×10^{-2} Torr. The sputtering current was maintained at 20 mA with a distance between the target and substrate of ~70 mm. To improve film uniformity, the

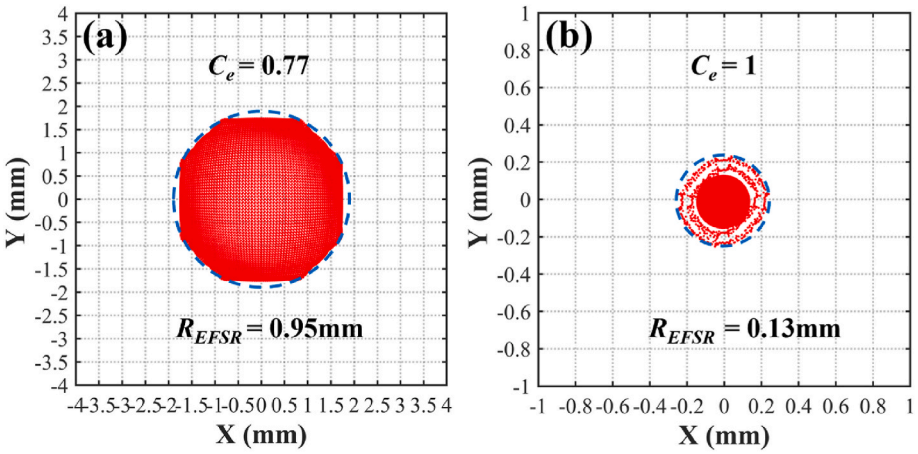

Fig. 3. Electron focal spot distribution on the anode surface: (a) before and (b) after optimization.

substrate was rotated at 18 rpm during deposition. Au photocathodes of varying thicknesses were fabricated by adjusting the sputtering time to 120, 150, 180, and 210 s, as illustrated in Fig. 4. The deposition rate was estimated from experimental data as ~6–8 nm/min.

3.2. Photocurrent measurements

Photocurrent was measured using a two-stage structure comprising an Au photocathode and a Cu anode, supported by ceramic components and separated by a 300-μm ceramic spacer. The spacer electrically insulated the negatively biased photocathode from the Cu anode, enabling reliable photocurrent collection. The structure was placed in a dynamic vacuum system capable of reaching a pressure of $\sim 10^{-7}$ Pa. Photocurrent was measured using a Keithley 6514 electrometer with two OPTAN-255 J-BL UV LEDs as the excitation source. Two UV LEDs were employed to provide sufficient optical power and to achieve uniform illumination across the photocathode. The LEDs emitted photons at 4.86 eV with a forward current of 100 mA and an average optical power greater than 1 mW. The photocurrents of the four Au photocathodes were measured in transmission mode. A diagram of the measurement circuit is shown alongside a photograph of the experimental setup in Fig. 5.

Fig. 6 shows the effects of $U_{cathode}$ and U_{led} on the anode current for deposition times of 120, 150, 180, and 210 s. As shown in Fig. 6(a), the anode current increased gradually with increasing $U_{cathode}$. When the bias reached approximately −100 V, nearly all cathode electrons were effectively collected, and the current increase slowed down, approaching saturation. This indicates that at this bias, the electric field between the cathode and anode sufficed to accelerate and collect photoelectrons efficiently. Fig. 6(b) shows that at $U_{cathode} = -100$ V, anode current increased significantly with U_{led}, which indicates that higher light intensity generated more photoelectrons. At $U_{led} = 6.7$ V and T = 150 s, the maximum anode current reached 20.45 nA. With longer deposition times, increased film thickness reduced both light transmittance and electron emission, which led to a significant decrease in photocurrent. When T = 150 s, the thickness of the resulting Au film was ~15–20 nm.

4. Fabrication and testing of MPPXT

4.1. Construction of prototype MPPXT

The MPPXT comprised five main components, including a light source, a photocathode, an MCP, a focusing electrode, and an anode assembly. The configuration of the power supply for each component is shown in Fig. 7(a). The distance between the light source and the photocathode was set to 10 mm to ensure full illumination of the effective photocathode area. The photocathode-MCP gap was set to 300 μm to form a close-coupled configuration, thereby improving electron injection into the MCP. This spacing was kept consistent with that used in the photocurrent measurements. The MCP-focusing electrode

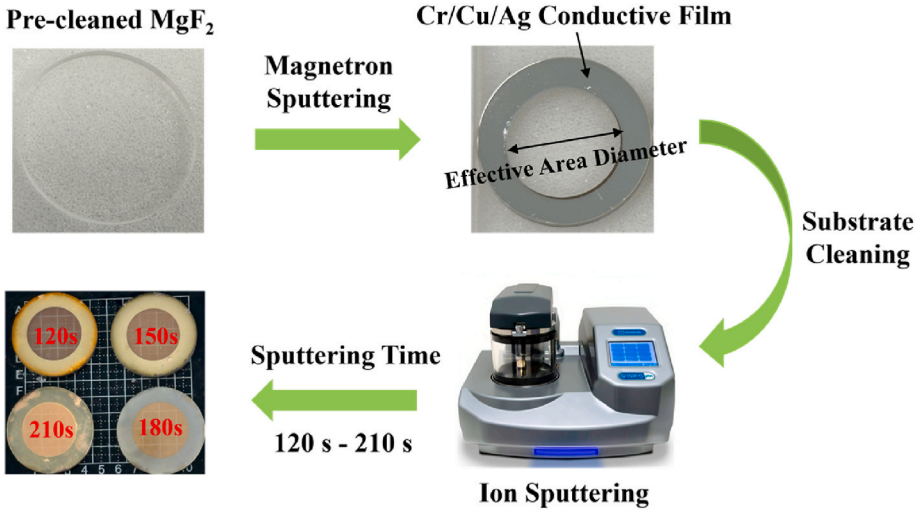

Fig. 4. Preparation process of Au photocathodes.

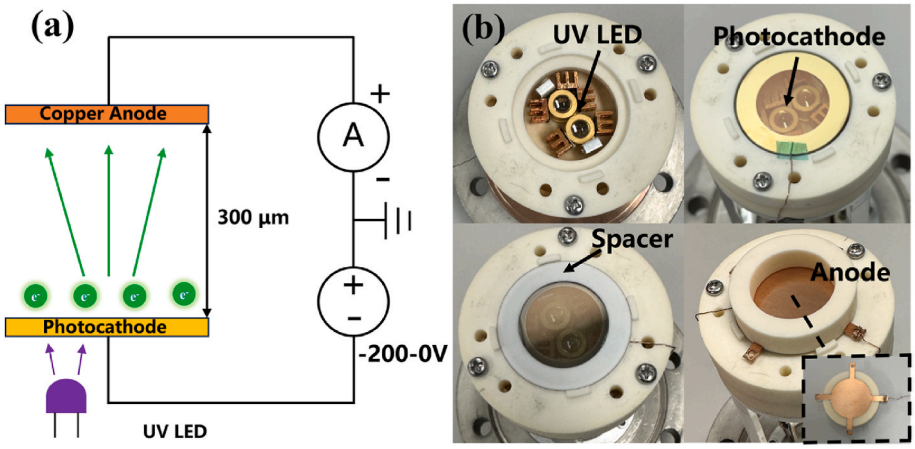

Fig. 5. (a) Photocurrent measurement circuit diagram. (b) Photograph of the experimental setup.

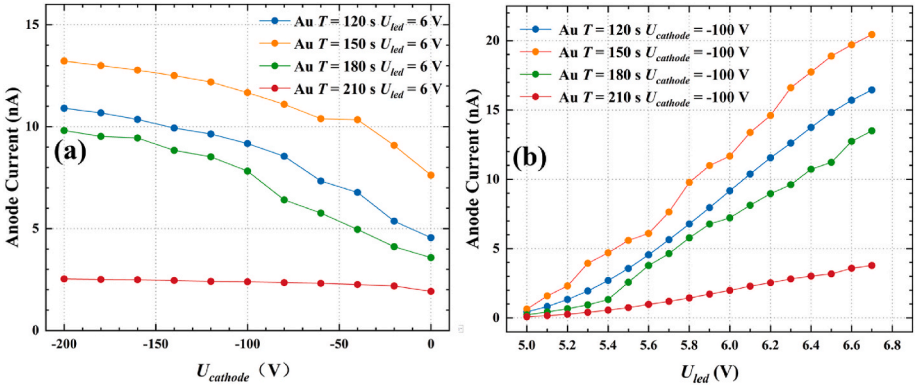

Fig. 6. Anode current as a function of (a) $U_{cathode}$ and (b) U_{led} for Au photocathodes with different deposition times.

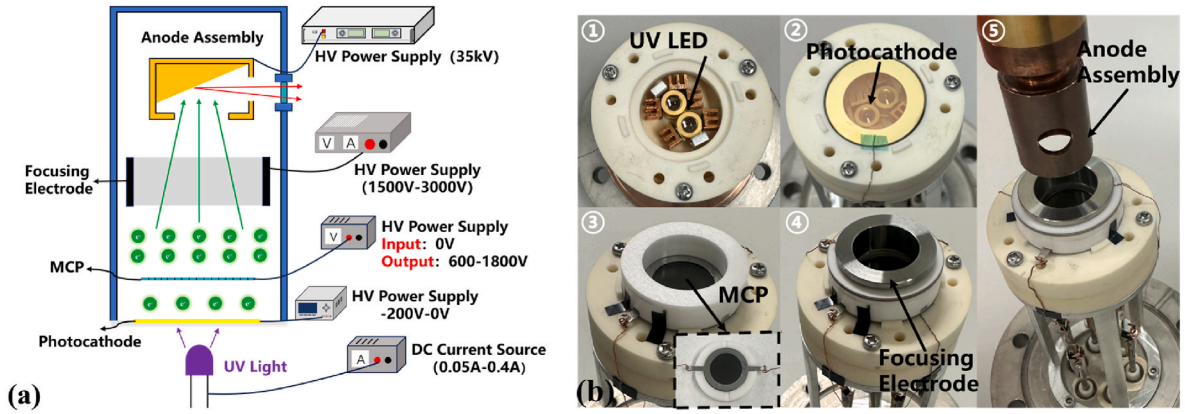

Fig. 7. (a) Power supply system of the MPPXT. (b) Photographs of the prototype and assembly process.

distance and the focusing electrode-anode assembly distance were set to 3.54 mm and 20 mm, respectively, according to the optimized design described in Section 2.2. Two 255-nm LEDs were used as the light source. The photocathode was prepared by ion-sputtering a 150 s Au thin film. The MCP had an effective diameter of 18.8 mm, a thickness of 0.4 mm, and channel diameter of 10 μm. To evaluate the influence of the number of installed MCPs on current gain, single- and dual-MCP configurations were compared. The focusing electrode was designed with a cup-shaped geometry with parameters as listed in Table 1. The anode assembly comprised an 18° reflective anode target and an anode shield. Based on this design, a prototype MPPXT was constructed and integrated into a dynamic vacuum system capable of maintaining pressure below 10^{-7} Pa. The prototype MPPXT is shown in Fig. 7(b). Electron and X-ray emission experiments were subsequently performed using this system.

4.2. Tube current and gain characteristics of MCPs

Fig. 8 shows the current–voltage characteristics of the MPPXT for single- and dual-MCP configurations at various U_{mcp}. During the measurements, U_{anode} was set to 15 kV, $U_{focusing}$ to 2300 V, and $U_{cathode}$ to −200 V. The UV LEDs were driven in continuous-wave (CW) mode. U_{led} was proportional to its optical output. High optical power increased

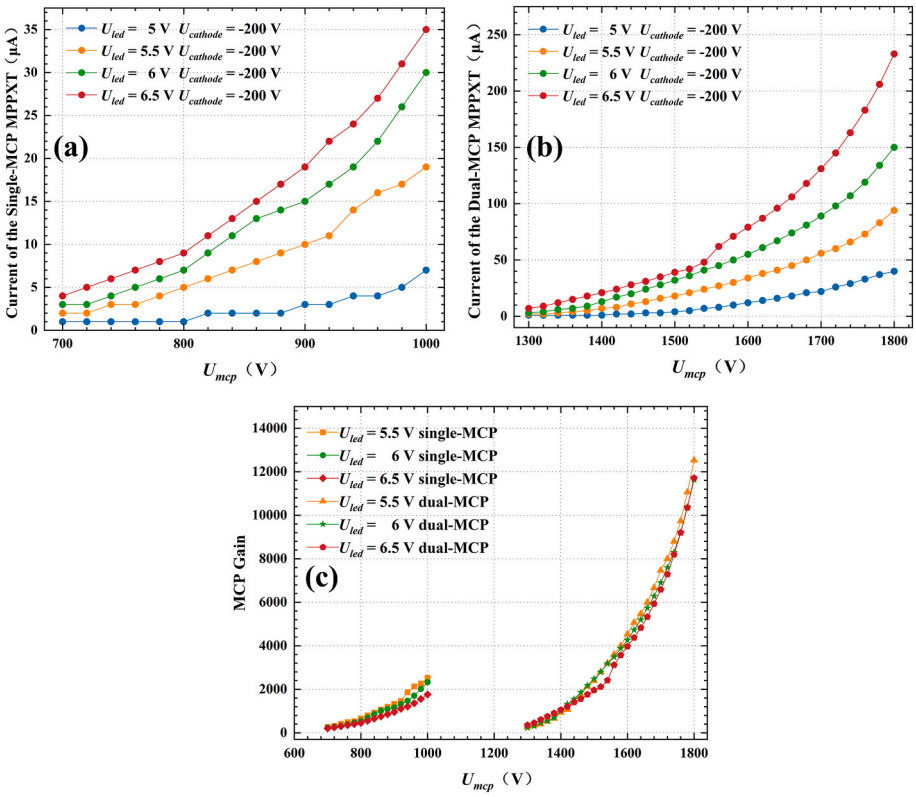

Fig. 8. Current characteristics of the MPPXT: (a) single-MCP. (b) dual-MCP. (c) Current gain characteristics of single- and dual-MCP configurations.

photocathode emission current and thus increased the tube current. As U_{mcp} increased, secondary electron multiplication within the MCP was amplified, which resulted in a pronounced increase in the tube current. The current gains in the single- and dual-MCP configurations at various U_{mcp} values were calculated as the ratio of the tube current to the corresponding photocathode current. Photocathode currents were measured from the Cu anode in the bipolar configuration described above. U_{led} = 5.5 V, 6.0 V, and 6.5 V corresponded to 7.5 nA, 12.9 nA, and 19.9 nA, respectively. The calculated current gains are shown in Fig. 8(c).

In both single- and dual-MCP configurations, a reduction in gain was observed with increasing cathode current (controlled by U_{led}). This effect was primarily attributed to the concentrated emission of photoelectrons, which confined the incident electron flux to a limited number of channels and produced a highly localized multiplication process. Excessive instantaneous electron flux within these channels exceeded the recharge rate of the channel walls, which reduced local fields, decreased secondary electron yield, and ultimately caused a notable degradation in total gain. For the single-MCP configuration at U_{mcp} = 1000 V, the tube current reached 35 μA, with a corresponding gain of ~1.76×10^3. In contrast, the dual-MCP configuration distributed the total gain between the two MCPs, allowing electrons multiplied in the first plate to spread laterally before entering the second plate, thus activating more channels. This spreading effect increased the overall multiplication efficiency and reduced the current load per MCP, which mitigated the local field collapse and maintained high secondary emission efficiency and operational stability. At U_{mcp} = 1800 V, the dual-MCP configuration achieved a tube current of 223 μA and a gain of ~1.17×10^4. Although a triple-MCP stack could, in principle, provide higher gain and output current, it would require a higher MCP bias voltage (U_{mcp}) and may be constrained by vacuum deterioration at elevated currents, which could compromise stable MCP operation. Moreover, introducing an additional MCP stage may increase temporal broadening and degrade timing performance. Accordingly, this study focused on comparing the single- and dual-MCP configurations. Within the tested range, the tube current increased continuously with U_{mcp} and no obvious gain saturation was observed. Based on this trend, higher output currents—potentially approaching the mA level—may be achievable by increasing the illumination intensity and/or U_{mcp}. However, this statement is a trend-based projection and requires further verification in future experiments under improved vacuum conditions.

4.3. Focal spot evaluation

The focal spot size of the MPPXT was evaluated using the star card method [23,24]. A 1° star card was used as the imaging object, and a flat-panel detector (Merak-1313, pixel size: 100 μm) served as the imaging device. The experimental setup is shown in Fig. 9(a). The experiment was performed with an anode voltage of 35 kV, a tube current of 20 μA, and a detector exposure time of 10 s. The source-to-object distance (SOD) and source-to-detector distance (SDD) were 16 and 24 cm, respectively. The resulting X-ray image is shown in Fig. 9(b).

Fig. 9(c)–(e) show the X-ray images of the star card at different $U_{focusing}$. These images were obtained by performing blur contour recognition processing on the image shown in Fig. 9(b). The blurred region (D, black shadow) formed during the imaging may be clearly observed. The blurred region D was primarily caused by the size and spatial distribution of the focal spot of the X-ray tube and represents a typical geometric artifact. A smaller D value indicates a smaller focal spot. The smallest D was observed at $U_{focusing}$ = 2300 V, which indicates an optimal focusing voltage of ~2300 V, which was consistent with the simulation results. Given those values for D and the magnification factor M [24], the minimum focal spot was calculated as ~0.27×0.47 mm, compared with the simulated value of 0.16×0.26 mm. The slight deviation from the simulation was likely due to assembly-induced tolerances and electron emission nonuniformity at the MCP exit, which may have broadened the D area and caused a marginal overestimation of the focal spot size.

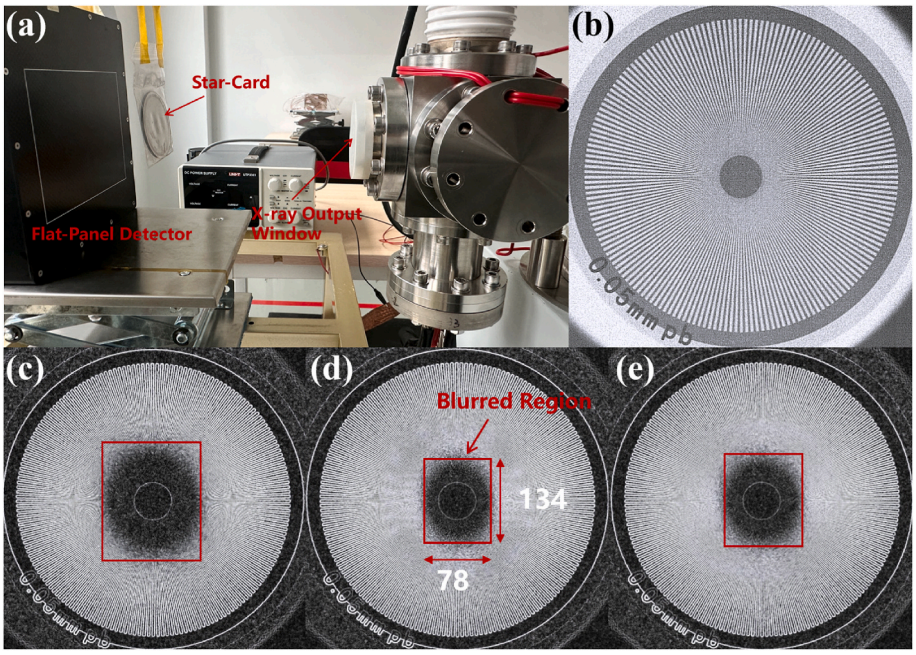

Fig. 9. (a) Experimental setup for X-ray imaging. (b) X-ray image of the star card (magnification relative to the actual object: M = 1.5). X-ray images of the star card showing the blurred region D under different $U_{focusing}$: (c) $U_{focusing}$ = 2100 V. (d) $U_{focusing}$ = 2300 V. (e) $U_{focusing}$ = 2500 V.

4.4. X-ray pulse emission characteristics

Benefiting from its photoexcitation mechanism, MPPXTs exhibit ultrafast response and enable precise control of X-ray intensity by modulating the light source. In this study, a signal generator was used to produce square-wave signals at various frequencies, which were then amplified using a power amplifier to drive the light source. The pulsed X-ray signals were detected and analyzed using a self-made yttrium-

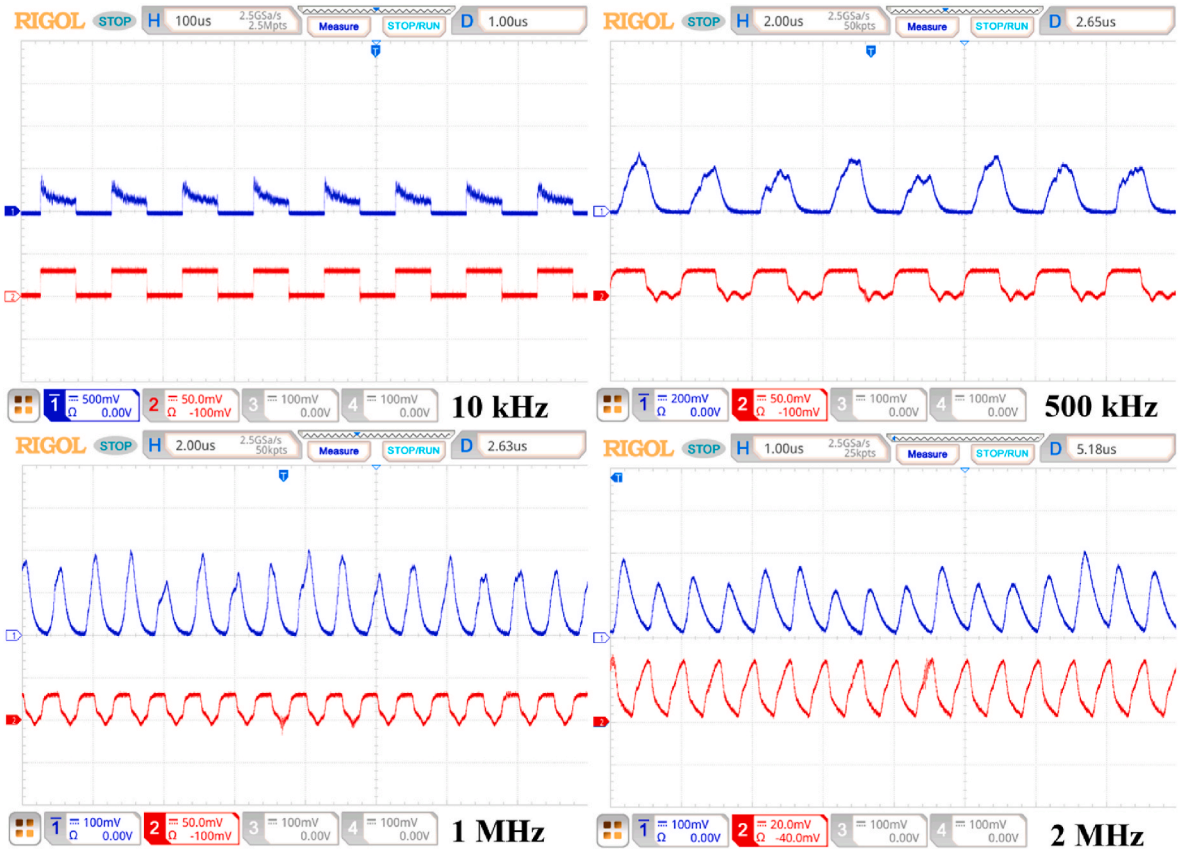

Fig. 10. X-ray pulse waveforms at various modulation frequencies. Red: driving signal applied to the light source. Blue: corresponding X-ray pulse signal. (For interpretation of the references to color in this figure legend, the reader is referred to the Web version of this article.)

lutetium oxyorthosilicate-silicon photomultiplier (LYSO-SiPM) coupled detector [25]. The results are presented in Fig. 10. At low modulation frequencies (red), the X-ray pulse signal (blue) exhibited significant differences in amplitude and good phase alignment with the input signal, with the waveform approximating a rectangular shape. As the modulation frequency increased to 2 MHz, the present LED driving chain (from the signal generator through the power amplifier to the LED) became limited by its bandwidth and could no longer maintain sharp rising and falling edges. Consequently, the optical modulation waveform was smoothed, and the detected X-ray waveform became approximately sinusoidal. Nevertheless, the high and low levels remained clearly distinguishable. In future work, the operating frequency could be further increased by replacing the power amplifier with a faster pulsed LED driver. A phase delay was also evident between the input and X-ray output signals, primarily due to the overall temporal response of the system.

To evaluate the tube current under pulsed excitation, a 50 % duty-cycle square-wave modulation was applied while maintaining the operating conditions used to obtain the maximum DC tube current of 223 μA ($U_{anode} = 15$ kV, $U_{focusing} = 2300$ V, $U_{cathode} = -200$ V, $U_{led} = 6.5$ V, $U_{mcp} = 1800$ V). The modulation frequency was set to 10 kHz, 500 kHz, 1 MHz, and 2 MHz, corresponding to pulse widths of 50 μs, 1 μs, 0.5 μs, and 0.25 μs, respectively. The time-averaged currents read back from the Wisman high-voltage power supply were 76 μA, 70 μA, 62 μA, and 59 μA at these frequencies. Because the current readback of the Wisman supply has limited bandwidth, these values represent the average tube current under pulsed operation rather than the instantaneous peak current.

5. Conclusion

In this study, we designed and implemented an MCP-based MPPXT and evaluated its performance experimentally. The size of the electron spot was reduced and the collection efficiency was improved by using a combined approach relying on CST and NSGA-II optimization. Experimental characterization showed a maximum photocurrent of 20.45 nA for the Au photocathode with a deposition time of 150 s. A prototype MPPXT was then fabricated based on the optimization results. Compared with the single-MCP configuration with a tube current of 35 μA, the dual-MCP configuration increased the tube current to 223 μA, which corresponded to a current gain of $\sim 1.17 \times 10^4$. This result demonstrates the considerable advantage of the proposed dual-MCP structure in enhancing electron multiplication. Imaging experiments demonstrated a minimum focal spot size of 0.27×0.47 mm at $U_{focusing} = 2300$ V, which was in close agreement with simulation results. The results of X-ray pulse testing demonstrated that the modulation bandwidth of the MPPXT system was 2 MHz with potential for further increase. Overall, the MCP-based MPPXT exhibited a high current gain, a small focal spot size, and high-speed modulation capabilities, which makes it promising for high-speed X-ray imaging and X-ray communication. Future efforts to increase the power of the light source, optimize photoelectron emission uniformity, or increase the MCP operating voltage are expected to further improve output current.

CRediT authorship contribution statement

Xiushan Wang: Writing – original draft, Visualization, Methodology, Formal analysis, Data curation. **Yunpeng Liu:** Supervision, Methodology, Funding acquisition, Conceptualization. **Kang Wang:** Writing – review & editing. **Ziyao Zeng:** Writing – review & editing. **Xiaobin Tang:** Writing – review & editing, Supervision, Resources.

Declaration of competing interest

The authors declare that they have no known competing financial interests or personal relationships that could have appeared to influence the work reported in this paper.

Acknowledgments

This work was supported by the National Natural Science Foundation of China (Grant No. 12375256).

Data availability

Data will be made available on request.

References

[1] Z. Feng, Y. Liu, J. Mu, W. Chen, S. Lai, X. Tang, Optimization and testing of groove-shaped grid-controlled modulated X-ray tube for X-ray communication, Nucl. Instrum. Methods Phys. Res. Sect. A Accel. Spectrom. Detect. Assoc. Equip. 1026 (2022) 166218, https://doi.org/10.1016/j.nima.2021.166218.
[2] X. Ma, B. Zhao, L. Sheng, Y. Liu, D. Liu, N. Deng, Grid-controlled emission source for space X-ray communication, Acta Phys. Sin. 63 (2014) 160701, https://doi.org/10.7498/aps.63.160701.
[3] S. Lai, X. Tang, Y. Liu, J. Mu, Z. Feng, K. Miao, X-ray high frequency pulse emission characteristic and application of CNT cold cathode x-ray source, Nanotechnology 33 (2022) 075201, https://doi.org/10.1088/1361-6528/ac378b.
[4] K. Miao, Y. Liu, S. Lai, J. Yin, F. Xiong, X. Dong, X. Tang, Emission characteristics of pulse CNT cold cathode X-ray source combined with channel electron multiplier, Appl. Radiat. Isot. 206 (2024) 111243, https://doi.org/10.1016/j.apradiso.2024.111243.
[5] Y. Zhao, Y. Chen, G. Zhang, D. Huang, R. Zhan, S. Deng, N. Xu, J. Chen, Pulsed voltage driving enhanced electron emission in ZnO nanowire cold cathode flat-panel X-ray source, Vacuum 199 (2022) 110970, https://doi.org/10.1016/j.vacuum.2022.110970.
[6] H. Xuan, Y. Liu, P. Qiang, T. Su, X. Yang, L. Sheng, B. Zhao, Light-controlled pulsed x-ray tube with photocathode, Chin. Phys. B 30 (2021) 118502, https://doi.org/10.1088/1674-1056/abff1e.
[7] H. Yu, Y. Liu, X. Wang, J. Mu, J. Bai, A. Xia, K. Wang, X. Tang, Design and testing of metal photocathode X-Ray source based on microchannel plate, IEEE Trans. Electron. Dev. 71 (2024) 7099–7104, https://doi.org/10.1109/TED.2024.3465463.
[8] S.E. Derenzo, W.W. Moses, S.C. Blankespoor, M. Ito, K. Oba, Design of a pulsed X-ray system for fluorescent lifetime measurements with a timing accuracy of 109 PS, Proc. IEEE Nucl. Sci. Symp. Med. Imag. Conf. 1 (1992) 117–119, https://doi.org/10.1109/NSSMIC.1992.301136.
[9] S.A. Rozhkov, V.V. Bakin, V.S. Rusetsky, D.A. Kustov, V.A. Golyashov, A.Y. Demin, H.E. Scheibler, V.L. Alperovich, O.E. Tereshchenko, Na_2KSb/Cs_xSb interface engineering for high-efficiency photocathodes, Phys. Rev. Appl. 22 (2024) 024008, https://doi.org/10.1103/PhysRevApplied.22.024008.
[10] W.G. Stam, M. Gaowei, E.M. Echeverria, K. Evans-Lutterodt, J. Jordan-Sweet, T. Juffmann, S. Karkare, J. Maxson, S.J. van der Molen, C. Pennington, P. Saha, J. Smedley, R.M. Tromp, Growth of ultra-flat ultra-thin alkali antimonide photocathode films, APL Mater. 12 (2024) 061114, https://doi.org/10.1063/5.0213461.
[11] G.A. Timofeev, N.N. Potrakhov, A.I. Nechaev, Experimental research of the x-ray communication system, in: Proc. 5th Int. Conf. on X-ray, Electrovacuum and Biomedical Technique, AIP Conf. Proc., 2019 020020, https://doi.org/10.1063/1.5095749, 2089.
[12] R. Zhang, Y. Li, T. Su, L. Sheng, Y. Liu, Q. Zhang, Y. Yan, Nanosecond scintillator decay time measurement using a pulsed X-ray source, in: Proc. 8th Int. Conf. on Material Strength and Applied Mechanics, IET Conf. Publ., 2025, https://doi.org/10.1049/icp.2025.2642.
[13] J. Schaber, R. Xiang, N. Gaponik, Review of photocathodes for electron beam sources in particle accelerators, J. Mater. Chem. C 11 (2023) 3162–3179, https://doi.org/10.1039/D2TC03729G.
[14] A. Lorusso, Overview and development of metallic photocathodes prepared by laser ablation, Appl. Phys. A 110 (2013) 869–875, https://doi.org/10.1007/s00339-012-7168-z.
[15] F. Anjum, H. Nasir, J. Lee, H.J. Kim, Fabrication and characterization of silver polycrystalline photocathode, Optik 269 (2022) 169906, https://doi.org/10.1016/j.ijleo.2022.169906.
[16] S.W. Lee, K. Attenkofer, D. Walters, M. Demarteau, Z. Yusof, Optimization of transmission mode metallic (aluminum) photocathodes, Phys. Procedia 37 (2012) 757–764, https://doi.org/10.1016/j.phpro.2012.03.726.
[17] X. Jiang, C.N. Berglund, A.E. Bell, W.A. Mackie, OS3: photoemission from gold thin films for application in multiphotocathode arrays for electron beam lithography, J. Vac. Sci. Technol. B 16 (1998) 3374–3379, https://doi.org/10.1116/1.590462.
[18] K.C. Gendreau, Z. Arzoumanian, S.J. Kenyon, N.S. Spartana, Miniaturized high-speed modulated X-ray source, U.S. Patent US9 117 (2015) 622 B2.
[19] C. Kamezawa, A. Cramer, W. Krull, W. Yashiro, K. Hyodo, R. Gupta, Dynamic X-ray elastography using a pulsed photocathode source, Sci. Rep. 11 (2021) 24128, https://doi.org/10.1038/s41598-021-03221-y.
[20] S. Hang, Y. Liu, H. Li, X. Tang, D. Chen, Temporal characteristic analysis of laser-modulated pulsed X-ray source for space X-ray communication, Nucl. Instrum.

Methods Phys. Res. Sect. A Accel. Spectrom. Detect. Assoc. Equip. 887 (2018) 18–26, https://doi.org/10.1016/j.nima.2018.01.031.
[21] K. Deb, A. Pratap, S. Agarwal, T. Meyarivan, A fast and elitist multiobjective genetic algorithm: NSGA-II, IEEE Trans. Evol. Comput. 6 (2002) 182–197, https://doi.org/10.1109/4235.996017.
[22] H. Yu, Y. Liu, J. Mu, J. Bai, A. Xia, X. Wang, X. Tang, X-ray tube design optimization methods based on CST particle studio, Appl. Radiat. Isot. 225 (2025) 112090, https://doi.org/10.1016/j.apradiso.2025.112090.
[23] J.D. Everson, J.E. Gray, Focal-spot measurement: comparison of slit, pinhole, and star resolution pattern techniques, Radiology 165 (1987) 261–264, https://doi.org/10.1148/radiology.165.1.3628780.
[24] J. Bai, Y. Liu, J. Mu, S. Lai, H. Yu, Optimization and testing of microfocus pulsed X-ray source, Nucl. Instrum. Methods Phys. Res. Sect. A Accel. Spectrom. Detect. Assoc. Equip. 1075 (2025) 170394, https://doi.org/10.1016/j.nima.2025.170394.
[25] Y. Liu, P. Dang, X. Tang, J. Mu, Z. Feng, Performance analysis of LYSO–SiPM detection module for X-ray communication during spacecraft reentry blackout, Nucl. Instrum. Methods Phys. Res. Sect. A Accel. Spectrom. Detect. Assoc. Equip. 1013 (2021) 165673, https://doi.org/10.1016/j.nima.2021.165673.